RSC Advances

PAPER

View Article Online
View Journal | View Issue



Cite this: *RSC Adv.*, 2017, **7**, 54594

# Ferromagnetic photocatalysts of $FeTiO_3$–$Fe_2O_3$ nanocomposites†

Baizhi Gao,[a] Caiping Yang,[a] Jun Chen,[a] Yuxing Ma,[a] Jiachen Xie,[a] Hao Zhang,[a] Lujun Wei,[b] Qi Li,*[a] Jun Du*[bc] and Qingyu Xu*[ac]

Besides harvesting sunlight over a broad wavelength range as much as possible, the efficient separation of photo-generated electron–hole pairs is vital for the development of high-quality photocatalysts. In this work, we design $FeTiO_3$ (FTO) and $Fe_2O_3$ (FO) nanocomposites ($x$FTO–(1 − $x$)FO), which are simply prepared using a hydrothermal method. The FTO is epitaxially grown on FO nanoparticles, and with the increasing concentration of FTO, the band gaps decrease from 2.43 eV ($x$ = 1.00) to 1.56 eV ($x$ = 0.60). The photocatalytic capability is significantly improved such that $x$FTO–(1 − $x$)FO ($x$ = 0.60) shows the highest value, which is about 8 times that of FO and 4 times that of FTO. Furthermore, strong ferromagnetism with saturated magnetization larger than 6 emu $g^{-1}$ is observed in $x$FTO–(1 − $x$)FO with $x \geq 0.60$. $x$FTO–(1 − $x$)FO ($x$ = 0.60) is further annealed at various temperatures. After annealing at 300 °C, the photocatalytic capability and ferromagnetism are both improved, by 38% and 31%, respectively, but drastically decrease with further increase of the annealing temperature to higher than 400 °C. The mechanism of the enhanced photocatalytic capability has been ascribed to the interdiffusion between FTO and FO at interfaces inside the nanocomposite particles, resulting in the formation of p–n junctions, which may facilitate the separation of photo-generated electron–hole pairs by the built-in-electric field. A significant enhancement of ferromagnetism occurs at the interdiffusion region with higher concentrations of FTO.

Received 6th October 2017
Accepted 22nd November 2017

DOI: 10.1039/c7ra11007c

rsc.li/rsc-advances



## Introduction

Photocatalysis is an environment-friendly energy transforming process from solar energy to chemical energy, which has attracted extensive research interest since the discovery of the first photocatalyst ($TiO_2$) used for water splitting in 1972.[1] However, the band gap of $TiO_2$ is 3.2 eV for the anatase phase and 3.0 eV for the rutile phase, which makes $TiO_2$ nearly inactive under visible light irradiation.[2–4] Many strategies were put forward for controlling the band gaps for better utilization of solar energy,[5] and improving carrier separation and transportation efficiency for enhancing chemical reactivity.[6,7] The formation of hetero-interfaces including p–n junctions[8–12] and Schottky contacts[4] has been proved to be very effective for carrier separation.[13] For p–n junctions, the generation of a built-in electric field at the interfaces by equaling the Fermi level leads to the transportation of electrons and holes in opposite directions and the recombination is therefore significantly suppressed.[14,15]

Based on the above-mentioned factors for high-performance photocatalyst, we develop a novel nanocomposite photocatalyst with $FeTiO_3$ (FTO) and α-$Fe_2O_3$ (FO), which has been proved to be a successful technique to develop efficient photocatalyst. The band gaps of FTO and FO are ~2.5 eV (ref. 16) and ~2.2 eV,[17,18] respectively. And FTO might have large adsorption and photocatalytic capability due to its easier formation of vacancy defects on the surface, which would both enhance the porous surface structure formation and $O_2$ diffusivity.[19] Although the above factors make them suitable to work under visible illuminations, their high carriers' recombination rate makes them not so efficient in practice.[17,18] This might be changed based on built-in-electric field in p–n junctions. It has been reported that opposite electrical properties can be achieved by changing the relative concentration in $FTO_x$–$FO_{(1-x)}$ (in molar ratio) solid solutions, with p-type for $x > 0.73$ and n-type for $x < 0.73$.[20] Thus, p–n junction might be formed at the interface of FTO and FO composites by proper interdiffusion. Furthermore, FTO and FO can form solid solution in full concentration range,[21,22] and strong ferromagnetism has been observed when FTO concentration is higher than 0.5, though pure FTO is antiferromagnetic.[23] Thus, this may further make $x$FTO–(1 − $x$)FO nanocomposites to be potential ferromagnetic photocatalysts, which can be magnetically separable for the efficient separation and recovery from treated water.[24–27]

[a]School of Physics, Southeast University, Nanjing 211189, China. E-mail: qli@seu.edu.cn; xuqingyu@seu.edu.cn

[b]School of Physics, Nanjing University, Nanjing 210093, China. E-mail: jdu@nju.edu.cn

[c]National Laboratory of Solid State Microstructures, Nanjing University, Nanjing 210093, China

† Electronic supplementary information (ESI) available. See DOI: 10.1039/c7ra11007c

In this paper, we simply prepared $x$FTO–(1 − $x$)FO nanocomposites by hydrothermal method. By carefully tuning the concentration of FTO, significantly enhanced photocatalytic capability with strong ferromagnetism has been observed, which has been confirmed to be due to the interdiffusion of FTO and FO at the interfaces inside the particles.

## Experimental

$x$FTO–(1 − $x$)FO nanocomposites ($x$ = 0.00, 0.20, 0.40, 0.60, 0.80 and 1.00 in molar ratio) were prepared by hydrothermal method.[21] Tetrabutylammonium hydroxide (TBAH, 40% aqueous solution), titanium isopropoxide (TTIP, 95% aqueous solution) and $FeSO_4 \cdot 7H_2O$ (99.9%) were used as the starting materials for the preparation of FTO, and KOH (99.9%) was used for the pH control. 0.005 mol TBAH (3.25 ml) was taken and diluted in 40 ml deionized water, and then 0.005 mol TTIP (1.5312 ml) was added rapidly. The mixture was stirred by a magnetic stirrer and kept at the temperature of 50 °C, until it was completely clear. 0.005 mol $FeSO_4 \cdot 7H_2O$ powder (1.39 g) was dissolved in 10 ml deionized water and immediately poured into the mixture which was kept on stirring. Then 0.05 mol KOH (2.805 g) was added into the mixture directly to adjust the pH value to 14. After that, the FO powders were added, and the amount was adjusted according to the designed composition. The stirring process was continued for another 20 min. The mixture was then moved to an autoclave. The autoclave was gradually heated to 220 °C in a speed of around 3–5 °C $min^{-1}$ and kept at 220 °C for 10 h, then slowly cooled down to room temperature. The precipitates were collected by centrifugation, washed by deionized water and ethanol. The washed products were finally dried at 70 °C for 3 h. Annealing process was performed at various temperatures for 3 hours. It must be noted that air should be isolated by the protection of Ar atmosphere in the whole preparation process.

The crystal structure was studied by $\theta$–$2\theta$ powder X-ray diffraction (XRD, Rigaku Smartlab3) using Cu K$\alpha$ radiation (1.5406 Å). The morphologies were studied by a scanning electron microscope (SEM, FEI Inspect F50), equipped with an energy dispersive X-ray spectroscope (EDX). Raman spectra were carried out on a Horiba Jobin Yvon LabRAM HR 800 micro-Raman spectrometer using a 532 nm laser. Band gaps were determined from the UV-vis diffuse reflectance spectrometer (DRS, Hitach U-3900). X-ray photoelectron spectroscopy (XPS) was carried out using an X-ray photoelectron spectrometer (ThermoFisher Scientific) with Al K$\alpha$ X-ray source ($h\nu$ = 1486.6 eV). The samples for XPS measurements were kept in the high-vacuum chamber overnight to remove the adsorbed air. Brunauer–Emmett–Teller (BET) specific surface areas were determined from $N_2$ adsorption by using an ASAP 2020 (Micrometrics USA) analyzer. The magnetic properties were measured by a vibrating sample magnetometer (VSM, Microsense EV7) with maximum applied field of 10 kOe. All the measurements were performed at room temperature.

The photocatalytic activities of the samples were tested by the photocatalytic decomposition of model contaminates, Rhodamine B (RhB), at room temperature with visible light irradiation. Typically, 50 mg of photocatalyst was dispersed in 150 ml of 2 mg $l^{-1}$ RhB aqueous solution. A 500 W Xe lamp (Beijing Trusttech Co Ltd, CHF-XM) equipped with a visible pass filter ($\lambda$ = 400–800 nm). The concentrations of RhB were monitored at 554 nm by using a UV-vis DRS (Hitach U-3900). A 30 min adsorption in darkness was applied as the pretreatment for absorption–desorption equilibrium before photocatalytic process.

## Results and discussion

Fig. 1 shows the XRD patterns of $x$FTO–(1 − $x$)FO nanocomposites. FTO and FO are both in corundum structure (space group $R\bar{3}$ for FTO and $R\bar{3}c$ for FO),[28] similar XRD patterns of pure phases can be observed for all the samples as shown in Fig. 1(a). A magnified view of (110) peaks is illustrated in the inset of Fig. 1(b). FTO has larger lattice constants than FO, thus the diffraction peaks gradually shift to smaller angles, as shown in Fig. 1(b), indicating the lattice expansion with increasing concentration of FTO calculated using Bragg's law. Interestingly,

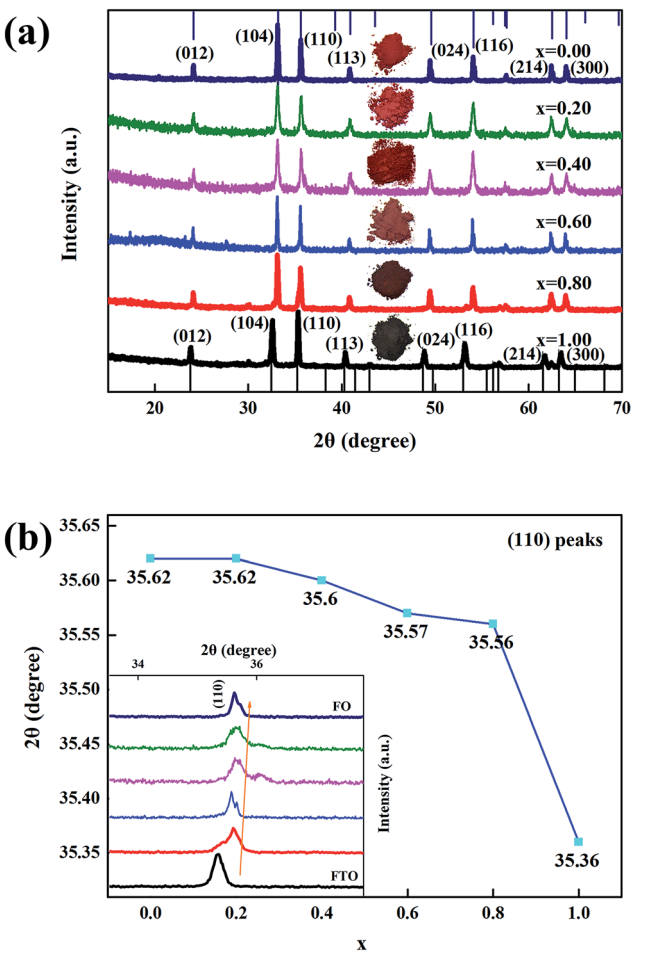


Fig. 1 (a) XRD patterns of $x$FTO–(1 − $x$)FO nanocomposites, the standard XRD patterns of FTO and FO are shown on the bottom and top, respectively. (b) The positions of (110) peaks in dependence on $x$. The inset in (a) shows the images of the powders, and inset of (b) shows the magnified view of (110) peaks.

a sudden shift of the diffraction peak can be observed between FTO and $x$FTO–$(1-x)$FO ($x = 0.80$), while the shift of the other peaks is much smaller in a nearly linear way. The sudden shift of the diffraction peaks from pure FTO to $x$FTO–$(1-x)$FO ($x = 0.80$) might be due to the epitaxial growth of FTO on FO particle surface, since FTO and FO have the similar crystalline structure. This can be evidenced by the observation of the superimposed peaks of (110) in $x$FTO–$(1-x)$FO ($x = 0.80$) from FO and FTO. In $x$FTO–$(1-x)$FO nanocomposites, FTO is grown on the surfaces of FO particles and the lattice of FTO is constrained by that of FO. With increasing $x$, the thickness of FTO layer increases, thus the lattice gradually relaxes, leading to the shift of diffraction peaks to smaller angle. For $x$FTO–$(1-x)$FO ($x = 0.80$), some FTO layers on FO particles are thick enough, and the lattice eventually relax to that of FTO. The crystallite size of $x$FTO–$(1-x)$FO calculated using Scherrer's equation is listed in Table S1 (ESI†), which is in the range between 40 nm and 60 nm. The images of $x$FTO–$(1-x)$FO powders are shown in inset of Fig. 1(a). As can be seen, the pure FTO powders shows gray black color, and FO shows red brown color. A gradual transformation between these two colors with variation of the relative concentration of FTO and FO can be clearly observed. This clearly confirms the coverage of FTO on FO.

Fig. 2 shows the morphologies of $x$FTO–$(1-x)$FO nanocomposites observed by SEM. As can be seen, the morphology of pure FTO particles are mainly nanodiscs (Fig. 2(f)), which is due to the predominantly exposed {0001} polar facets.[21,29] With only slight introduction of FO with concentration of 0.20, the morphology changes drastically to particle, which is quite similar with the morphology of FO particles. This can be understood by the mechanism of epitaxial growth of FTO on FO particles, which wraps the surfaces of FO particles. And a fully wrapped morphology can be clearly seen in $x$FTO–$(1-x)$FO ($x = 0.80$) in Fig. 2(e), which is in agreement with its XRD pattern. The exact concentration of FTO and FO in the nanocomposites is further measured by EDX, and the results are listed in Table 1. It can be clearly seen that the atomic ratio between Fe and Ti is very close to 1 for pure FTO. However, slight deviation between the measured concentration and designed concentration of FTO in the nanocomposites can be observed, which might be due to the slight fluctuation in ratios of starting materials and incomplete fabrication of FTO during hydrothermal process. For simplicity, the designed concentration of FTO is used in the paper to denote each sample.

The structures of $x$FTO–$(1-x)$FO nanocomposites were further studied by Raman Spectra and UV-vis DRS, and the results are shown in Fig. 3. It has been reported that the Raman spectra of FO have two $A_{1g}$ modes (225 and 498 $cm^{-1}$) and five $E_g$ modes (247, 293, 299, 412, and 613 $cm^{-1}$).[30] The five Raman modes corresponding to FO can be clearly resolved, which locate at 216, 280, 400, 490, and 600 $cm^{-1}$. With increasing $x$, the peak position shows little variation, indicating that the preparation process has little influence on the structure of FO particles. It can also be seen that no extra Raman modes can be observed with increasing $x$. This might be due to that the Raman signal from FTO is quite weak, leading to the coverage of small peaks by noises. Furthermore, most of the Raman modes of FTO are close to those of FO, and the peaks are quite broad, which makes them difficult to be separated.[31] However, a peak locating at 673 $cm^{-1}$ corresponding to the $A_g$ Raman mode of FTO can be clearly resolved in the Raman spectrum of FTO.[29] In contrast to the nearly unshifted Raman modes from FO, a clear shift to lower wavenumber (664 $cm^{-1}$) can be observed in $x$FTO–

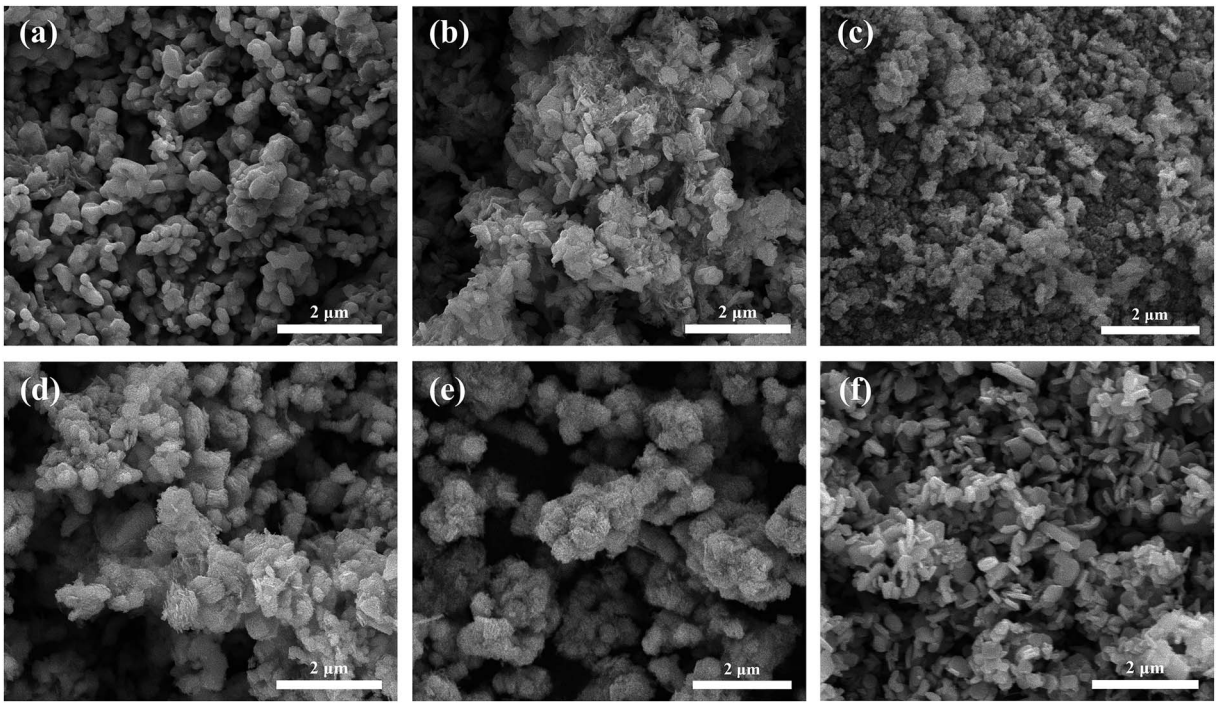


Fig. 2 (a), (b), (c), (d), (e) and (f) are SEM images of $x$FTO–$(1-x)$FO with $x = 0.00$, 0.20, 0.40, 0.60, 0.80, 1.00, respectively.

 

Table 1 The measured concentration of $x$FTO–(1 − $x$)FO nanocomposites by EDX

| Samples ($x$FTO–(1 − $x$)FO) | $x = 1.00$ | $x = 0.80$ | $x = 0.60$ | $x = 0.40$ | $x = 0.20$ |
|---|---|---|---|---|---|
| Fe $K$ (%) | 50.74 | 55.16 | 72.72 | 81.82 | 89.10 |
| Ti $K$ (%) | 49.26 | 44.84 | 27.28 | 18.18 | 10.90 |
| Measured ratio (Fe/Ti) | 1.03 | 1.23 | 2.67 | 4.50 | 8.17 |
| Measured $x$ | — | 0.90 | 0.55 | 0.36 | 0.22 |

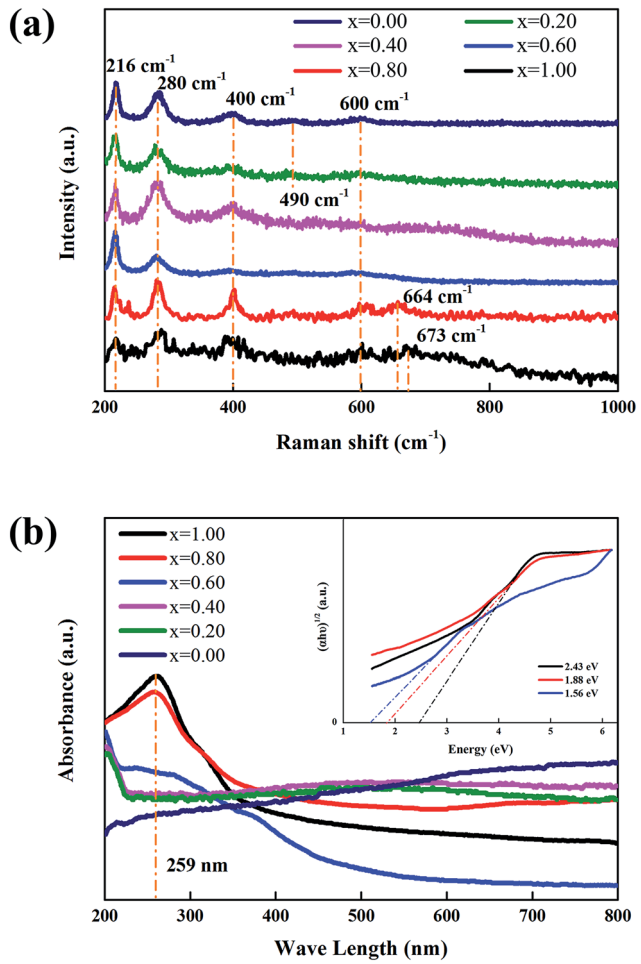


Fig. 3 (a) Raman spectra, and (b) UV-vis DRS of $x$FTO–(1 − $x$)FO nanocomposites. The inset in (b) shows the curve fitting by Kubelka–Munk function.

(1 − $x$)FO ($x = 0.80$) for this mode of FTO. It has been reported that this mode of FTO corresponds to Ti–O stretching motion, which can qualitatively reflect the distortion of $TiO_6$.[31] This can be understood by the growth of FTO on FO particle surface, which induces lattice strain in FTO due to the epitaxial growth.

The band gaps were determined by UV-vis DRS patterns, as shown in Fig. 3(b). It can be clearly seen that nanocomposites of $x \leq 0.40$ show nearly constant absorbance in the full visible light range, which means that the band gap cannot be determined in this method.[17,22] Only for the nanocomposites of $x \geq 0.60$, a clear absorption edge can be resolved. The optical absorption near the band edge of a semiconductor often obeys the Kubelka–Munk equation: $(\alpha h\nu)^n = A(h\nu - E_g)$,[33,34] where $A$ is a constant, $h\nu$ is the photon energy, $E_g$ is the band gap of the semiconductor, $\alpha$ is the absorption coefficient, and $n$ is 0.5 for indirect band gap materials, such as FTO.[32] It has been reported that there are direct and indirect band gaps for FO.[35] We fitted the absorbance curves of nanocomposites of $x \geq 0.60$ using Kubelka–Munk equation with $n = 0.5$ and 2, and found the best fit can be obtained by using $n = 0.5$ (indirect band gap for FTO), as shown in the inset of Fig. 3(b). This is understandable that FTO takes the main absorption of light in the nanocomposites with high FTO concentration due to the main coverage of FTO on FO particle surfaces. And this can also be explained as FTO particles have lower reflectance than FO, which plays a more important role in the absorption of light in nanocomposites.[21] The band gap for FTO is ~2.43 eV, which is consistent with the previous reported value of ~2.5 eV.[17,20] With decreasing $x$ in the nanocomposites, the band gaps decrease to 1.88 eV ($x = 0.80$) and 1.56 eV ($x = 0.60$), leading to an enhanced absorption capability of light through a broader wavelength range.[17]

The valence states of Fe and Ti of nanocomposites ($x = 0.00$, 0.60, 0.80 and 1.00) was studied by XPS as in Fig. 4. The C 1s peak (284.8 eV) is used for charge correction. It is reported that the binding energy of $Fe^{2+}$, $Fe^{3+}$, $Ti^{3+}$ and $Ti^{4+}$ are 709.0 eV, 711.0 eV, 457.1 eV and 458.6 eV, respectively,[36,37] which have been used for peak fittings. The Fe 2p spectra are shown in Fig. 4(a)–(d) from $x = 0.00$, 0.60, 0.80 and 1.00, respectively. As can be seen, with the introduction of FTO, the $2p_{3/2}$ peaks shift to lower binding energy from 711.0 eV for $Fe^{3+}$ to 709.0 eV for $Fe^{2+}$.[32] From the peak fitting of $2p_{3/2}$ fitting, an obviously varied proportion is observed, which is in agreement with the measured ratios of $x$FTO–(1 − $x$)FO nanocomposites. The results are shown in Table S2 (ESI†). The Ti 2p spectra are shown in Fig. 4(e)–(g) for $x = 0.60$, 0.80 and 1.00, respectively. There is only slight fluctuation of the proportion of $Ti^{3+}$ and $Ti^{4+}$ due to the different samples with slightly fluctuated fabricating conditions of FTO. Since XPS is a very sensitive surface technique with depth limitation of about 5 nm, the concentration of $Fe^{2+}$ will increase drastically and be much higher than $x$ due to the coverage of FTO on FO particles without interdiffusion. Thus the XPS results clearly confirm the interdiffusion between FTO and FO.

Photocatalytic efficiencies were measured by decomposing RhB as model contaminant under a visible light illumination at room temperature.[38,39] The typical time-dependent UV-vis spectra of RhB solution decomposed by $x$FTO–(1 − $x$)FO ($x = 0.60$) in photochemical reaction is shown in Fig. 5(a). The intensity of the characteristic absorption peak of RhB solution decreases with

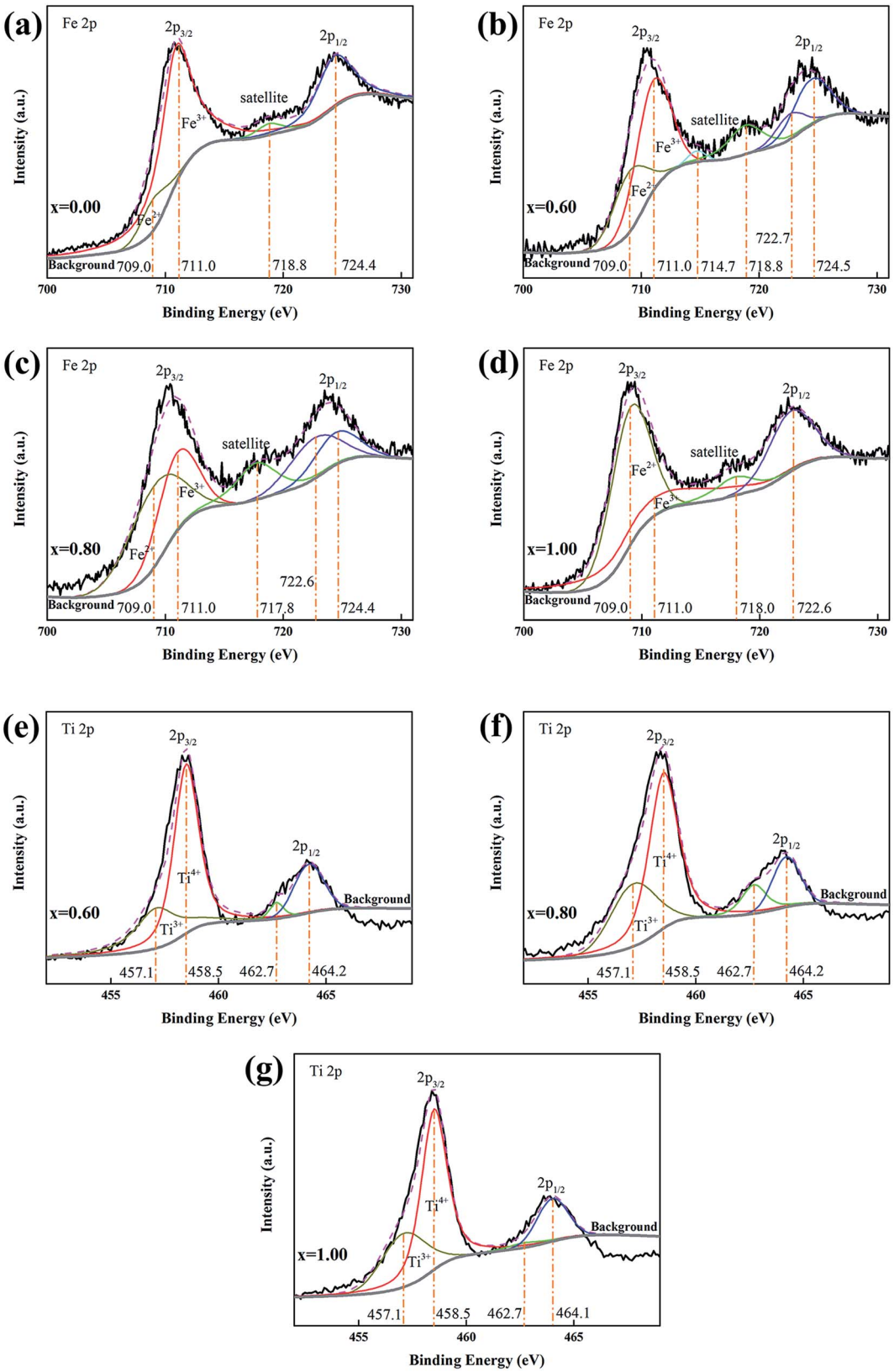


Fig. 4 The XPS spectra of the nanocomposites forth Fe 2p of (a), (b), (c) and (d) for $x = 0.00, 0.60, 0.80, 1.00$, respectively, and Ti 2p spectra of (e), (f) and (g) for $x = 0.60, 0.80, 1.00$, respectively.

time. The absorption peak position shifts to shorter wavelength, revealing the mechanism of *N*-deethylation mechanism in the photochemical reaction.[40] Photocatalytic processes for the degradation of RhB aqueous solutions using $x$FTO–$(1-x)$FO are shown in Fig. 5(b). It can be clearly seen that $x$FTO–$(1-x)$FO ($x = 0.60$) shows the highest photocatalytic capability. After 5 h, about 90% RhB was degraded. For better comprehension of kinetics of the RhB degradation, the fitting using pseudo-first-order model $(\ln(C/C_0)) = Kt$, where $t$ is the irradiation time and $K$ is the reaction coefficient, is drawn in Fig. 5(c). The reaction coefficient $K$ calculated from the slope of the curves is illustrated in Fig. 5(d). The highest value of $K$ of 0.375 is obtained for $x$FTO–$(1-x)$FO ($x = 0.60$), which is almost 8 times of FO (0.048), and 4 time of FTO (0.086). The decrease of $K$ for $x = 0.80$ sample can be explained as excessive coverage of FO particles by FTO, which might impede photo-generated electrons in FO to participate the reaction. Furthermore, the conductivity of $x$FTO–$(1-x)$FO solid solutions has been studied, and the resistivity is minimum when $x$ is between 0.50 and 0.60.[20] This indicates the highest electric conductivity for $x$FTO–$(1-x)$FO ($x = 0.60$), which is beneficial for the photocatalytic activity. The specific surface area of $x$FTO–$(1-x)$FO ($x = 0.60$) (14.966 $m^2\ g^{-1}$) is smaller than that of FTO (24.554 $m^2\ g^{-1}$), excluding the contribution of surface area on the improvement of photocatalytic capability (Fig. S1, ESI†). We further prepared the mechanically mixed powder of FTO and FO with molar ratio same to $x$FTO–$(1-x)$FO ($x = 0.60$), the photocatalytic capability is only similar to pure FTO and FO (Fig. S2, ESI†), indicating the important role of the interface region in the $x$FTO–$(1-x)$FO ($x = 0.60$) nanocomposites. Due the inorganic nature of our composites and photocatalytic operation at room temperature, the good recycling ability can be expected.[41,42]

The field dependent magnetization (M – H) curves for $x$FTO–$(1-x)$FO were measured by VSM, as shown in Fig. 6. Clear hysteresis loops can be observed, indicating the ferromagnetic nature. The saturated magnetization ($M_{sat}$) in dependence on $x$ is plotted in the inset of Fig. 6(a). With $x \leq 0.40$, only weak ferromagnetism with small $M_{sat}$ is observed. While $x$ is larger than 0.60, strong ferromagnetism with large $M_{sat}$ can be seen. Similar phenomenon has been reported by Y. Ishikawa *et al.*[23] Interestingly, considerably strong ferromagnetism is also observed for pure FTO, which is in contrasts to its antiferromagnetic nature.[23] This might be due to the O deficiency observed by XPS, which can significantly enhance the ferromagnetism in FTO.[23] The strongly enhanced ferromagnetism in solid solution of FTO and FO with FTO concentration higher than 50% mainly comes from $Fe^{2+}$ ions and the magnetic moments of $Fe^{3+}$ ions are canceled each other out.[43] However, the saturated magnetization of $x$FTO–$(1-x)$FO is much smaller than that of solid solution with the same concentration. For example, $M_{sat}$ for solid solution with $x = 0.60$ is larger than 150 emu $cm^{-3}$, which is about 30 emu $g^{-1}$ (considering the average

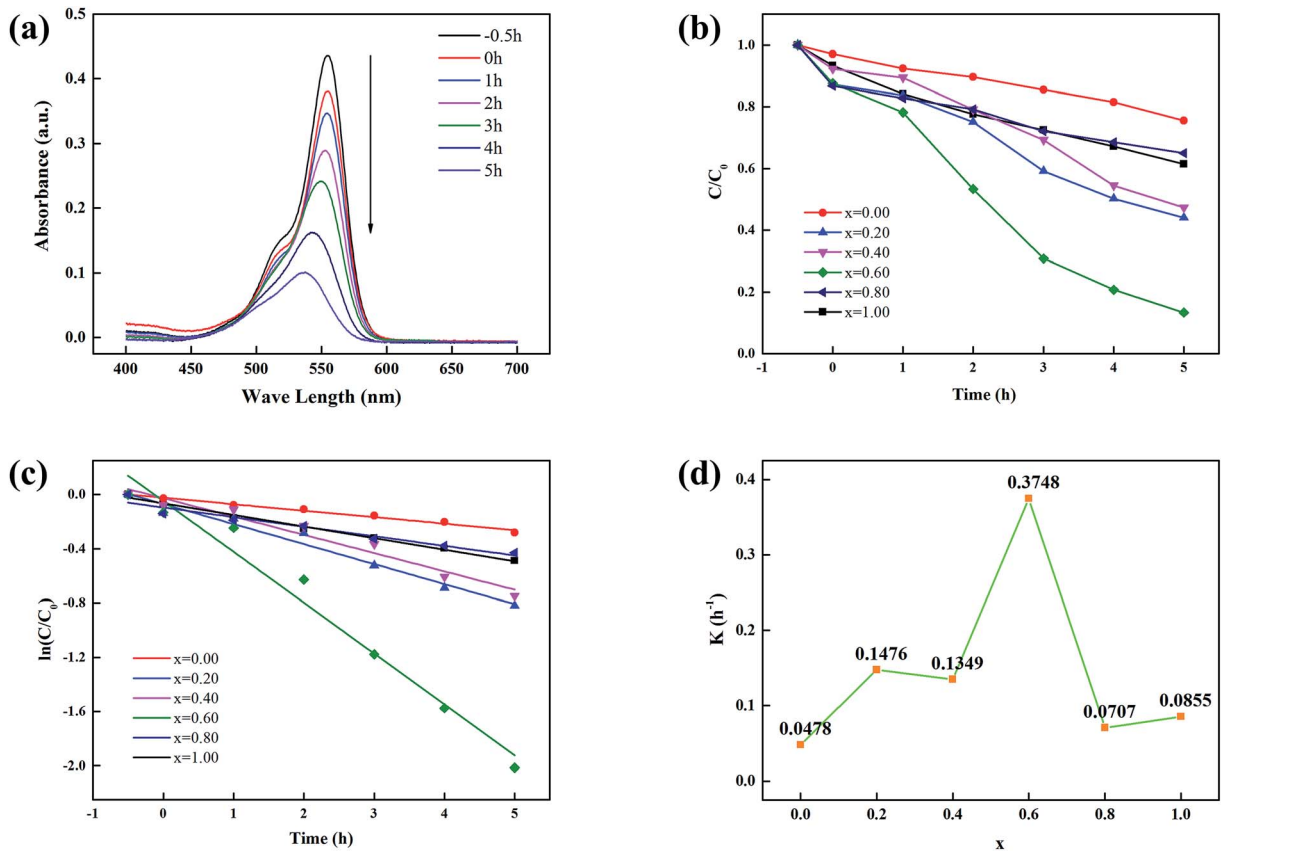


Fig. 5 (a) Absorption spectra for the degradation of RhB using $x$FTO–$(1-x)$FO ($x = 0.60$). (b) The photocatalytic performances of $x$FTO–$(1-x)$FO under visible irradiation. (c) The pseudo-first-order kinetics fitting. (d) The reaction efficiency in dependence on $x$.

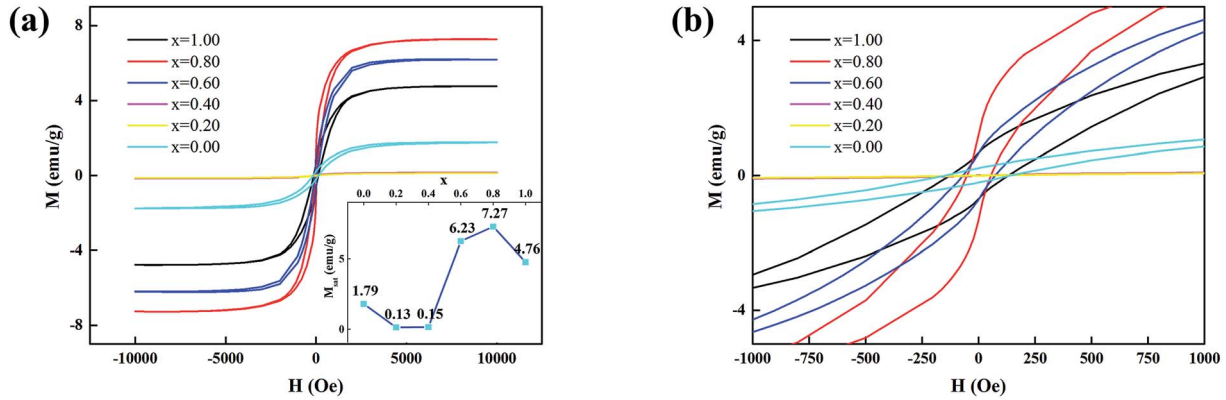


Fig. 6 (a) M − H curves, and (b) the enlarged view of M − H curves for *x*FTO–(1 − *x*)FO. The inset in (a) shows the dependence of saturated magnetization on *x*.

mass density of about 5 g cm$^{-3}$), while $M_{sat}$ of *x*FTO–(1 − *x*)FO (*x* = 0.60) is only 6.3 emu g$^{-1}$. Thus, we can conclude that in the as-prepared *x*FTO–(1 − *x*)FO, interdiffusion happens and solid solution forms at interface region between FTO and FO with varying FTO concentration from high at FTO side to low at FO side. The wasp-waist shape M − H curves shown in the magnified view of low field in Fig. 6(b) (*x* = 0.80, red) is due to the superposition of M − H curves of the solid solution with varying FTO concentration, which has various coercivities.[44]

To further improve the interdiffusion at the interface between FTO and FO, annealing was performed to *x*FTO–(1 − *x*)FO (*x* = 0.60), which shows the best photocatalytic capability. The XRD patterns show that no observable changes can be observed with annealing temperature increased up to 700 °C (Fig. S3†). The SEM images show that the roughly wrapped surface with FTO nanoparticles on FO particles disappears and becomes smooth, which is similar to FO (Fig. S4†). This indicates that the increasing annealing temperature improves the interdiffusion between FTO and FO. Raman spectra were also studied that no obvious difference appears among the annealed samples, in agreement with XRD (Fig. S5†). The valence states of Fe 2p and Ti 2p of annealed sample of *x* = 0.60 at 300 °C and 700 °C were tested. No obvious change of valence states can be observed at 300 °C. But it shows a significant transformation of $Fe^{2+}$ + $Ti^{4+}$ to $Fe^{3+}$ + $Ti^{3+}$ at 700 °C (Fig. S6†).[21] This might be induced by many reasons including interdiffusion, valence states transfer in FTO and O defects, which is not involved in our discussion. The photocatalytic capability was measured for the annealed samples by degradation of RhB (Fig. S7†). With increasing the annealing temperature to 300 °C, the reaction coefficient K is further increased to 0.52, and abruptly drops with further increasing annealing temperature above 400 °C, as shown in Fig. 7(a). Interestingly, the magnetic properties show the similar dependence on annealing temperature, as shown in Fig. 7(b). With increasing annealing temperature to 300 °C, $M_{sat}$ increases to 8.1 emu g$^{-1}$, which is about 31% increment. With further increasing annealing temperature, $M_{sat}$ then decreases (Fig. S8†).

This significant enhanced photocatalytic capability has been observed for *x*FTO–(1 − *x*)FO (*x* = 0.60) annealed at 300 °C, which is 6 times of FTO and 11 times of FO, with strong room temperature ferromagnetism, which makes it a potential ferromagnetic photocatalyst. To understand the mechanism, a schematic diagram is shown in Fig. 8. Due to the interdiffusion at the interface between FTO and FO inside the nanocomposite particles, solution with high concentration of FTO

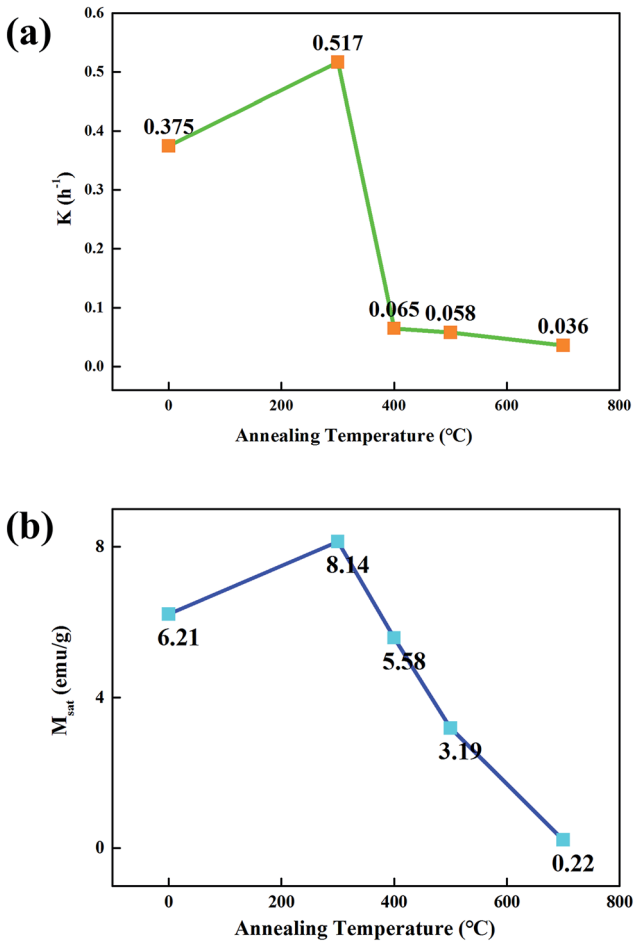


Fig. 7 (a) The reaction coefficient *K*, and (b) saturated magnetization $M_{sat}$ of *x*FTO–(1 − *x*)FO (*x* = 0.60) annealed at various temperatures.

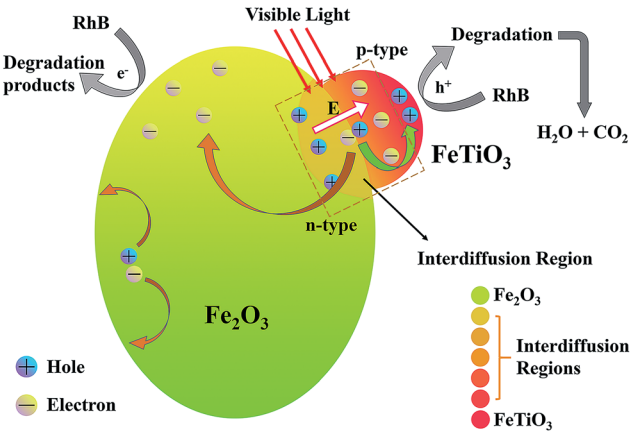


Fig. 8 The schematic diagram of the mechanism of enhanced photocatalytic capability for the nanocomposites.

and low concentration of FTO forms at the interface. It has been reported that electric conductivity of FTO and FO solid solution shows p-type for FTO concentration higher than 73% and n-type for FTO concentration lower than 73%.[20] Thus, p–n junction may form at the interface region, which induces the built-in-electric field at the interface. The electric field may facilitate the separation of the photon-generated electron–hole pairs and avoid the recombination,[15] which improves the photocatalytic capability. And due to the existence of FTO–FO solid solution at the interface with high FTO concentration, significantly enhanced ferromagnetism can be observed.[23] The proper annealing may enlarge the interdiffusion region of FTO and FO nanocomposites, which provides a larger separating region. Thus, larger amounts of photon-generated carriers may participate in the reaction without recombination. And the enlarged interdiffusion region with high FTO concentration may further increase the ferromagnetic properties. However, with further increasing annealing temperature, the interdiffusion may induce the uniform distribution of FTO in FO, which may destroy the p–n junction. Thus, the separation of electrons and holes is weakened. Furthermore, the solid solution with high concentration of FTO decreases, leading to the decreases of magnetization.[23]

## Conclusions

In conclusion, $x$FTO–$(1-x)$FO nanocomposites were prepared using hydrothermal method. The structural characterization indicates the epitaxial growth of FTO on the surface of FO particles. The band gap decreases from 2.43 eV ($x = 1.00$) to 1.56 eV ($x = 0.60$), which broadens the absorption wavelength range. The photocatalytic capability has been significantly improved. $x$FTO–$(1-x)$FO ($x = 0.60$) shows the highest reaction coefficient, which is about 8 times of FO and 4 times of FTO. Furthermore, strong ferromagnetism has been observed for $x$FTO–$(1-x)$FO with $x \geq 0.60$, up to 7.27 emu $g^{-1}$ ($x = 0.80$). The photocatalytic capability and ferromagnetism of $x$FTO–$(1-x)$FO ($x = 0.60$) are both further improved by over 30% after annealing at 300 °C, but drastically decrease with further increasing the annealing temperature. The mechanism has been ascribed to the interdiffusion between FTO and FO at interfaces inside the nanocomposite particles. The solid solution with various FTO concentrations at interface region is formed by interdiffusion, leading to the formation of p–n junction, which may facilitate the separation of photon-induced electron–hole pairs by the built-in-electric field. The strong ferromagnetism comes from the solid solution at interdiffusion regions with higher concentration of FTO.

## Conflicts of interest

There are no conflicts to declare.

## Acknowledgements

This work is supported by the National Natural Science Foundation of China (51771053, 51471085), the Natural Science Foundation of Jiangsu Province of China (BK20151400, BK20140054), and the open research fund of Key Laboratory of MEMS of Ministry of Education, Southeast University.

## References

1 A. Fujishima and K. Honda, *Nature*, 1972, **238**, 37–38.
2 A. Manikandan, E. Manikandan, B. Meenatchi, S. Vadivel, S. K. Jaganathan, R. Ladchumananandasivam, M. Henini, M. Maaza and J. S. Aanand, *J. Alloys Compd.*, 2017, **723**, 1155–1161.
3 N. C. S. Selvam, A. Manikandan, L. J. Kennedy and J. J. Vijaya, *J. Colloid Interface Sci.*, 2013, **389**, 91–98.
4 D. Maruthamani, S. Vadivel, M. Kumaravel, B. Saravanakumar, B. Paul, S. S. Dhar, A. Habibi-Yangjeh, A. Manikandan and G. Ramadoss, *J. Colloid Interface Sci.*, 2017, **498**, 449–459.
5 Z. S. Wang, Y. Cui, K. Hara, Y. Dan, C. Kasada and A. Shinpo, *Adv. Mater.*, 2007, **19**, 1138–1141.
6 Z. Zhao, H. Liu and S. Chen, *Nanoscale*, 2012, **4**, 7301–7373.
7 Q. D. Truong, J. Y. Liu, C. C. Chung and Y. C. Ling, *Catal. Commun.*, 2012, **19**, 85–89.
8 X. Meng, Z. Li, H. Zeng, J. Chen and Z. Zhang, *Appl. Catal., B*, 2017, **210**, 160–172.
9 Y. Yuana, Z. Yub, Y. Li, H. Lu, X. Chen, W. Tu, Z. Ji and Z. Zou, *Appl. Catal., B*, 2016, **181**, 16–23.
10 H. Li, Y. Sang, S. Chang, X. Huang, Y. Zhang, R. Yang, H. Jiang, H. Liu and Z. Wang, *Nano Lett.*, 2015, **15**, 2372–2379.
11 X. Meng and Z. Zhang, *J. Photochem. Photobiol., A*, 2015, **310**, 33–44.
12 X. Yu, J. Zhang, Z. Zhao, W. Guo, J. Qiu, X. Mou, A. Li, J. P. Claverie and H. Liu, *Nano Energy*, 2015, **16**, 207–217.
13 H. Wang, L. Zhang, Z. Chen, J. Hu, S. Li, Z. Wang, J. Liu and X. Wang, *Chem. Soc. Rev.*, 2014, **43**, 5234–5244.
14 L. Li, P. A. Salvador and G. S. Rohrer, *Nanoscale*, 2014, **6**, 24.
15 H. Wang, L. Zhang, Z. Chen, J. Hu, S. Li, Z. Wang, J. Liu and X. Wang, *Chem. Soc. Rev.*, 2014, **43**, 5234.

16 G. Rollmann, A. Rohrbach, P. Entel and J. Hafne, *Phys. Rev. B: Condens. Matter Mater. Phys.*, 2004, **69**, 165107.
17 D. S. Ginley and M. A. Butler, *J. Appl. Phys.*, 1977, **48**, 5.
18 M. Mishra and D. Chun, *Appl. Catal., A*, 2015, **498**, 126–141.
19 L. Qin, Z. Cheng, J. A. Fan, D. Kopechek, D. Xu, N. Deshpande and L. Fan, *J. Mater. Chem. A*, 2015, **3**, 11302.
20 Y. Ishikawa, *J. Phys. Soc. Jpn.*, 1958, **13**, 1.
21 Y. J. Kim, B. Gao, S. Y. Han, M. H. Jung, A. K. Chakraborty, T. Ko, C. Lee and W. I. Lee, *J. Phys. Chem. C*, 2009, **113**, 19179–19184.
22 X. Zhang, T. Li, Z. Gong, H. Zhao, L. Wang, J. Wan, D. Wang, X. Li and W. Fu, *J. Alloys Compd.*, 2015, **653**, 619–623.
23 Y. Ishikawa and S. Akimoto, *J. Phys. Soc. Jpn.*, 1957, **12**, 10.
24 C. Barathiraja, A. Manikandan, A. M. U. Mohideen, S. Jayasree and S. A. Antony, *J. Supercond. Novel Magn.*, 2016, **29**, 477–486.
25 V. M. Teresita, A. Manikandan, B. A. Josephine, S. Sujatha and S. A. Antony, *J. Supercond. Novel Magn.*, 2016, **29**, 1691–1701.
26 A. Manikandan, M. Durka, K. Seevakan and S. A. Antony, *J. Supercond. Novel Magn.*, 2015, **28**, 1405–1416.
27 D. K. Manimegalai, A. Manikandan, S. Moortheswaran and S. A. Antony, *J. Supercond. Novel Magn.*, 2015, **28**, 2755–2766.
28 R. J. Harrison and S. A. T. Redfern, *Phys. Chem. Miner.*, 2001, **28**, 399–412.
29 X. Guang, J. Zheng, M. Zhao, L. Li and G. Li, *RSC Adv.*, 2013, **3**, 13635.
30 D. L. A. Faria, S. V. Silva and M. T. Oliveira, *J. Raman Spectrosc.*, 1997, **28**, 873.
31 X. Wu, S. Qin and L. Dubrovinsky, *J. Solid State Chem.*, 2010, **183**, 2483.
32 D. Gu, Y. Qin, Y. Wen, L. Qin and H. J. Seo, *J. Taiwan Inst. Chem. Eng.*, 2017, **78**, 431.
33 B. Meenatchi, V. S. Lakshmi, A. Manikandan, V. Renuga, A. Sharmila, K. R. N. Deve and S. K. Jaganathan, *J. Inorg. Organomet. Polym.*, 2017, **27**, 446–454.
34 S. Suguna, S. Shankar, S. K. Jaganathan and A. Manikandan, *J. Supercond. Novel Magn.*, 2017, **30**, 691–699.
35 C. S. Garoufalis, P. Poulopoulos, N. Bouropoulos, A. Barnasas and S. Baskoutas, *Phys. E*, 2017, **89**, 67.
36 T. Yamashita and P. Hayes, *Appl. Surf. Sci.*, 2008, **254**, 2441–2449.
37 M. C. Biesinger, L. W. M. Lau, A. R. Gerson and R. S. C. Smart, *Appl. Surf. Sci.*, 2010, **257**, 887–898.
38 A. Manikandan, E. Hema, M. Durka, M. A. Selvi, T. Alagesan and S. A. Antony, *J. Inorg. Organomet. Polym.*, 2015, **25**, 804–815.
39 G. Mathubala, A. Manikandan, S. A. Antony and P. Ramar, *J. Mol. Struct.*, 2016, **1113**, 79–87.
40 Q. Wang, C. Chen, D. Zhao, W. Ma and J. Zhao, *Langmuir*, 2008, **24**, 7338–7345.
41 Y. Guo, G. Zhang, J. Liu and Y. Zhang, *RSC Adv.*, 2013, **3**, 2963.
42 S. Sivakumar, A. Selvaraj, A. K. Ramasamy and V. Balasubramanian, *Water, Air, Soil Pollut.*, 2013, **224**, 1529.
43 H. Hojo, K. Fujita, H. Ikeno, T. Matoba, T. Mizoguchi, I. Tanaka, T. Nakamura, Y. Takeda, T. Okane and K. Tanaka, *Appl. Phys. Lett.*, 2014, **104**, 112408.
44 A. A. Cristóbal, C. P. Ramos, P. G. Bercoff, P. M. Botta and J. M. P. López, *Mater. Chem. Phys.*, 2012, **133**, 971.